Kent Academic Repository

Song, Fenhong, Zhang, Ruibo, Chu, Wanlong, Tan, Zengqiang, Ma, Long, Fan, Jing, Wang, Gang, Qi, Qi and Cao, Yang (2026) *Interfacial Charge-Transfer Enhancement via High-Entropy Alloy Regulated MXene Heterostructures for Asymmetric Supercapacitor Applications.* Energy & Environmental Materials . ISSN 2575-0356.

RESEARCH ARTICLE

Energy & Environmental Materials WILEY

Electrode Materials, Supercapacitor

Interfacial Charge-Transfer Enhancement via High-Entropy Alloy Regulated MXene Heterostructures for Asymmetric Supercapacitor Applications

Fenhong Song, Ruibo Zhang, Wanlong Chu, Zengqiang Tan, Long Ma, Jing Fan, Gang Wang, Qi Qi, and Yang Cao**

MXenes exhibit exceptional chemical properties, which are primarily attributed to their diverse surface functional groups and tunable elemental composition. Chemical intercalation is commonly used to address interlayer stacking and improve MXene conductivity. Meanwhile, high-entropy alloys (HEAs) are a groundbreaking category of materials with broad compositional flexibility that provide multiple active sites, facilitating electrochemical redox reactions in supercapacitors. Synergistically combining MXenes with HEAs offers significant potential for developing advanced energy storage technologies. Herein, a CrMnFeCoNi-based HEA was successfully synthesized and doped with a $Ti_3C_2F_2$ MXene through a hydrothermal approach. In a single-electrode setup with a 1 M potassium hydroxide electrolyte, the prepared HEA@MXene exhibited an impressive specific capacitance of 872 F g^{-1} at a current density of 1 A g^{-1}. Moreover, an asymmetric device constructed from this material exhibited an energy density of 72.66 Wh kg^{-1} at a power density of 640 W kg^{-1}. Theoretical investigations using density functional theory (DFT) revealed that HEA integration enhances MXene conductivity and promotes hydroxide adsorption in solution, thereby improving supercapacitor performance.

1. Introduction

The escalating demand for high-performance, fast-response energy storage systems has driven extensive research into supercapacitors. These devices bridge the gap between conventional capacitors and batteries by offering high power density and long cycle life.[1] However, their relatively low energy density remains a key limitation for broader application. Constructing asymmetric supercapacitors (ASCs) with advanced electrode materials is a predominant strategy to simultaneously enhance both energy and power metrics.[2] In this context, the performance of ASCs is fundamentally governed by the intrinsic properties and structural design of their electrode materials.[3]

The design of high-performance supercapacitor electrodes necessitates the optimization of key parameters, including conductivity, specific surface area, pore structure, and electrochemical reactivity, to enhance charge–discharge efficiency and stability.[4] In this pursuit, advanced materials like MXenes and high-entropy alloys (HEAs) offer a novel design paradigm. MXenes, for instance, are prized for their excellent metallic conductivity, hydrophilicity, and mechanically robust layered structures that provide abundant charge storage sites, making them promising for long-term, stable operation.[5,6] Meanwhile, HEAs, which comprise five or more near-equimolar elements, leverage their configurational entropy and "cocktail effect."[7,8] This results in lattice distortion, a homogeneous distribution of transition metals, and abundant active sites, which collectively enhance redox kinetics, conductivity, and cyclability.[9]

Notably, the great potential of HEAs has been demonstrated in composites with carbon matrices, such as with carbon nanotubes (rHEA-CNT)[10,11] or graphene oxide (CrCoFeNi-GO),[12] for enhanced supercapacitor performance.[13] Parallelly, the high-entropy concept has been successfully applied to MXenes, leading to materials known as high-entropy MXenes, which also show promising electrochemical properties.[14–16] Etman et al.[17] successfully synthesized a $Ti_{1.1}V_{0.7}Cr_xNb_{1.0}Ta_{0.6}C_3T_z$ high-entropy MXene for utilization in acidic supercapacitors. More innovatively, $Ti_{1.1}V_{0.7}Cr_xNb_{1.0}Ta_{0.6}C_3T_z$ was employed in zinc-ion hybrid supercapacitors and lithium-ion batteries, achieving both high capacity and excellent stability.[18] These studies show that combining high-entropy materials with MXenes can greatly enhance electrochemical performance.

In the context of MXene-based composites, the integration of transition metal oxides has been widely investigated to address MXene restacking and introduce pseudocapacitance: $Fe_2O_3@Ti_3C_2$ composites realize expanded interlayer spacing and pseudocapacitive contribution from Fe^{2+}/Fe^{3+} redox reactions, yet their specific capacitance is limited

---

Prof. F. Song, R. Zhang, W. Chu, Prof. L. Ma, Prof. J. Fan, G. Wang
School of Energy and Power Engineering, Northeast Electric Power University, Jilin 132012, China
E-mail: crystalfan@neepu.edu.cn
Dr. Z. Tan
Xi'an Thermal Power Research Institute Co., Ltd., Xi'an 710054, China
Dr. Q. Qi
School of Engineering, University of Kent, Canterbury, Kent CT2 7NT, UK
Prof. Y. Cao
Department of Mechanical Engineering, The University of Hong Kong, Hong Kong, China
E-mail: yangcao1@connect.hku.hk

The ORCID identification number(s) for the author(s) of this article can be found under https://doi.org/10.1002/eem2.70426.

DOI: 10.1002/eem2.70426

to 213 F g^{-1} at 0.5 A g^{-1},[19] while Bi_2O_3-decorated MXene nanocomposites alleviate layer agglomeration but suffer from insufficient cycling stability due to weak interfacial bonding between metal oxides and MXene substrates.[20] Although such MXene–metal oxide systems can introduce pseudocapacitance and act as interlayer spacers, their performance is restricted by the single redox site of metal oxides, easy agglomeration of oxide nanoparticles, and poor interfacial electron transfer.[21] These limitations that HEAs can be potentially overcome via their multi-element synergistic effect.

However, most prior efforts have focused on integrating HEAs with carbon matrices or fabricating high-entropy MXenes, and even the well-studied MXene-metal oxide composites suffer from intrinsic limitations. In contrast, HEA@MXene integration can construct unique synergistic heterostructures that surpass both individual components and traditional MXene-based composites. In such heterostructures, MXene scaffolds inhibit HEA nanoparticle agglomeration and accelerate electron transport, while HEA particles serve as efficient spacers to mitigate MXene restacking and provide multi-element redox sites for enhanced pseudocapacitance, thus overcoming the single redox site and weak interfacial bonding issues of MXene-metal oxide systems. Therefore, this highlights the critical need for systematic investigations into the rational fabrication of HEA@MXene heterostructures and a fundamental understanding of their interfacial charge-transfer behavior.

This study reports the first synthesis of an HEA@MXene nanohybrid via a simple, one-pot hydrothermal process for utilization as an advanced electrode material in ASCs. The highly conductive MXene served as a scaffold, enabling the nucleation of HEAs and promoting the formation of a nanosheet structure, which enhanced the conductivity of the resulting nanohybrid material. In a single-electrode system with 1 M KOH electrolyte, the HEA@MXene nanohybrid demonstrated a high specific capacitance of 872 F g^{-1} at 1 A g^{-1}. The prepared ASC device exhibited an energy density of 72.66 Wh kg^{-1} and excellent retention at a power density of 640 W kg^{-1}. Finally, DFT was used to compute the density of states and the differential charge, providing a detailed analysis of the functionality of this supercapacitor.

2. Results and Discussion

2.1. Structural, Morphological, and Compositional Characterization

The preparation steps for obtaining HEA@MXene are schematically shown in **Figure** 1a. First, the HEA was prepared by induction melting, and the particle size was refined by high-energy ball milling. Next, the HEA powder was composited with a single layer of MXene via a hydrothermal reaction to obtain the HEA@MXene composite with a core-shell structure. XRD analysis of the HEA and HEA@MXene samples is presented in Figure 1b. The distinct diffraction peaks observed at 43.9°, 51.2°, and 75.4° can be indexed to the (111), (200), and (220) planes of a face-centered cubic (FCC) lattice, respectively. To unambiguously confirm the formation of a single-phase solid solution, Rietveld refinement was performed on the XRD pattern (Figure S1, Table S1, Supporting Information). The refinement results revealed an excellent fit with the standard card for an FCC-structured $Fe_{0.496}Mn_{0.253}Ni_{0.251}$ alloy (PDF# 04-006-8209). The pronounced shift in peak positions relative to any pure constituent metal is attributed to the significant lattice distortion induced by the incorporation of multiple principal elements (Cr, Mn, Fe, Co, Ni) with differing atomic radii. Both the successful refinement against a single-phase model and the observable peak shifts conclusively demonstrate the formation of a monophase FCC high-entropy alloy solid solution.[22] A series of HEA@MXene composites was synthesized via a hydrothermal method by combining MXene with varying masses (0.02, 0.05, and 0.08 g) of HEA. Slow-scan XRD patterns collected over 5–10° for the 5-HEA@MXene (Figure S2a, Supporting Information) composite clearly show the characteristic diffraction peak of $Ti_3C_2T_x$ MXene, and the XRD pattern of bare $Ti_3C_2T_x$ after hydrothermal treatment (Figure S2b, Supporting Information) confirms that mild hydrothermal treatment at 180 °C only induces partial surface oxidation of MXene to TiO_2 without complete structural conversion, as the moderate temperature restricts oxidation primarily to the surface while preserving the bulk $Ti_3C_2T_x$ framework.[23,24] At low HEA loadings, the composite is dominated by these TiO_2 peaks derived from MXene oxidation. Only when the added mass of HEA precursors reaches 0.08 g do obvious diffraction peaks assigned to high-entropy alloy oxides emerge, indicating the successful formation of well-crystallized HEA oxide phases under this composition.

The FTIR spectra of MXene and HEA@MXene are shown in Figure 1c. The broad peak at 3000–3500 cm^{-1} was ascribed to the -OH functional groups on the MXene surface. The H peak near 1630 cm^{-1} was attributed to H-OH bending vibrations, while the peaks at 1116 cm^{-1} and 1630 cm^{-1} corresponded to C-F and C-O stretching vibrations, respectively. The peak at 625 cm^{-1} was ascribed to Ti-F stretching vibrations (characteristic of MXene materials). In the FTIR spectrum of HEA@MXene, new peaks at 962 and 504 cm^{-1} were ascribed to metal oxides and metal-fluoride bonds, and the Ti-F bond peak migrated to 665 cm^{-1}.[25]

Figure 1d shows that BET tests were carried out on the three HEA@MXene composites. Each of these materials demonstrates type IV isotherm characteristics, featuring pronounced H4-type hysteresis loops across the relative pressure (P/P0) range of 0.4–0.8, indicating a composite pore structure comprising both micropores and slit-like mesopores. Among them, the 5-HEA@MXene sample shows the highest nitrogen adsorption capacity and the most pronounced hysteresis loop, corresponding to the largest BET specific surface area of 75.09 m^2 g^{-1}. This value is considerably higher than those of the 2-HEA@MXene and 8-HEA@MXene samples, which have specific surface areas of only 44.16 and 26.46 m^2 g^{-1}, respectively.

The pore size distribution analysis further corroborates these findings (Figure 1e). The 5-HEA@MXene sample exhibits a sharp and intense dV/dD peak in the 2–5 nm mesopore range, signifying a highly concentrated and well-developed mesoporous system.[26] In contrast, the 8-HEA@MXene sample shows a substantially weakened dV/dD peak and a shrunken hysteresis loop, suggesting that excessive HEA loading leads to pore blockage or structural collapse, consistent with its drastically reduced surface area.

As shown in Figure 1f, DOS for HEA, MXene, and HEA@MXene exceeded 0 at the Fermi level, indicating their metallic conductivity. Notably, HEA@MXene exhibited significant accumulation near the Fermi level. To provide a quantitative comparison, the integrated DOS values near the Fermi level were calculated. The values for pristine MXene, HEA, and the HEA@MXene composite are approximately 20.0, 43.2, and 67.7 eV, respectively. This clear numerical increase confirms the enhanced electronic state density in the composite compared to its individual components. As shown in the partial wave density of states diagram in Figure 1g, all five metals in the HEA demonstrated strong

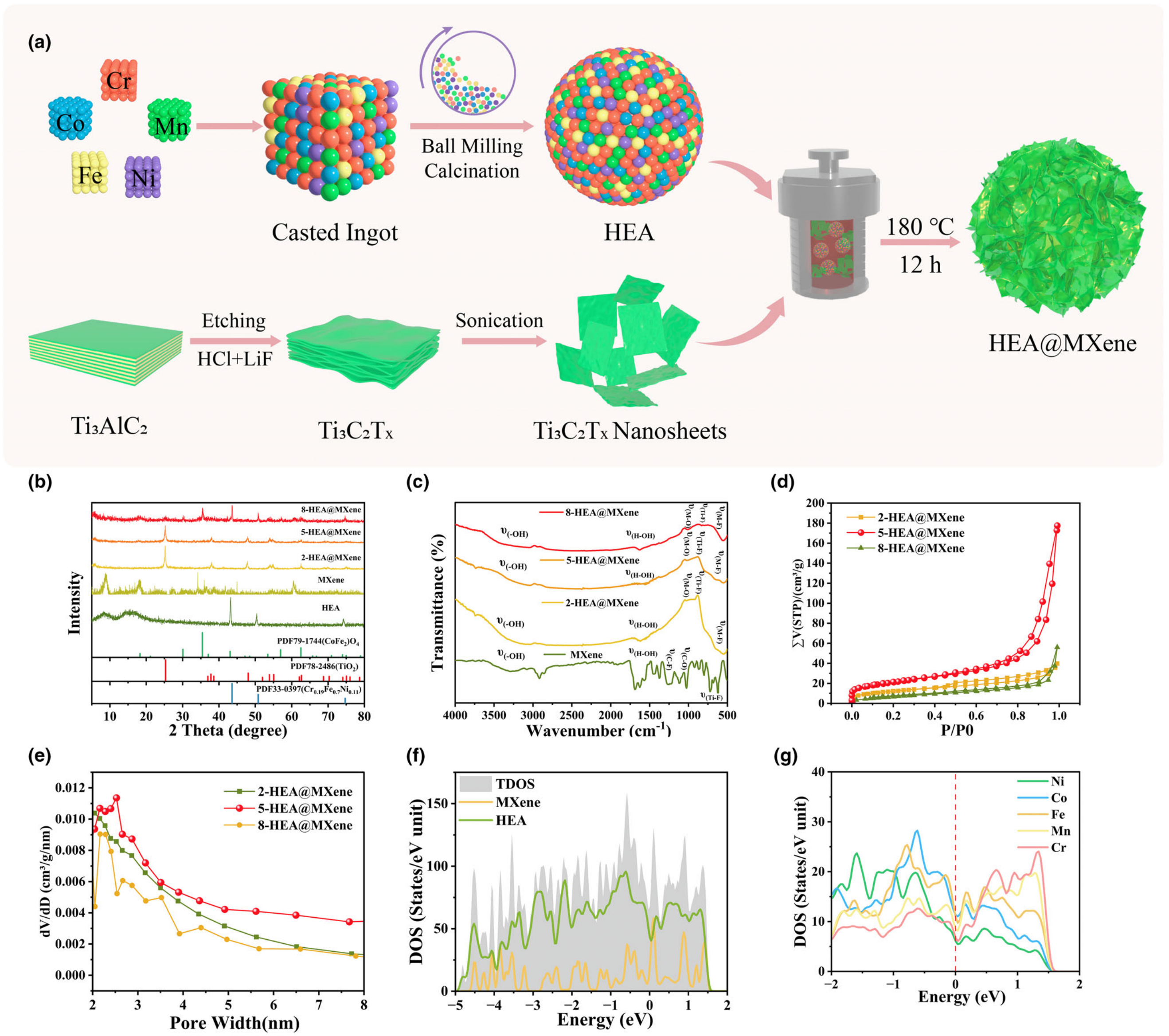

Figure 1. a) Schematic diagram showing preparation of HEA@MXene; b) powder XRD patterns of HEA, MXene, and HEA@MXene; c) FTIR spectra; d) N_2 adsorption–desorption isotherms of HEA@MXene; e) pore size distributions of HEA@MXene; f) DOS of HEA@MXene; g) partial density of states.

electrical conductivity in the HEA@MXene composite, indicating their practical contributions to the conduction of electrons. The d orbitals of cobalt offer higher electronic states than those of other metals, thereby enhancing the overall conductivity of the composite.[27] The DOS values of a material reflect its energy-storage capacity and electronic-transport performance. When the HEA@MXene heterostructure was formed, the arrangement and interaction patterns of the electronic energy levels significantly affected the overall DOS, which was higher than those of HEA and MXene. This significantly impacted their electrical conductivity.

HEA, MXene, and HEA@MXene samples were analyzed by SEM, as shown in **Figure** 2a. After etching, the MXene sample showed a clear lamellar structure, with the MXene lamellae appearing as relatively complete monolayers. As shown in Figure 2b, the prepared HEA particles had irregular shapes with smooth surfaces. Figure 2c–f shows a low-magnification SEM image of HEA@MXene; it clearly shows HEA particles wrapped by MXene nanosheets, visually confirming a core-shell heterostructure. Figure 2f shows a higher-magnification view of a single particle, confirming the core-shell structure of HEA@MXene, with HEA cores encapsulated by MXene sheets. This well-defined architecture was consistently observed in the 2-HEA@MXene and 5-HEA@MXene samples, where the MXene sheets effectively wrapped the HEA particles. In contrast, the 8-HEA@MXene sample (Figure 2d) exhibited compromised morphology; the MXene surface showed notable wrinkles, and some of the HEA particles had detached. Based on the laser particle size

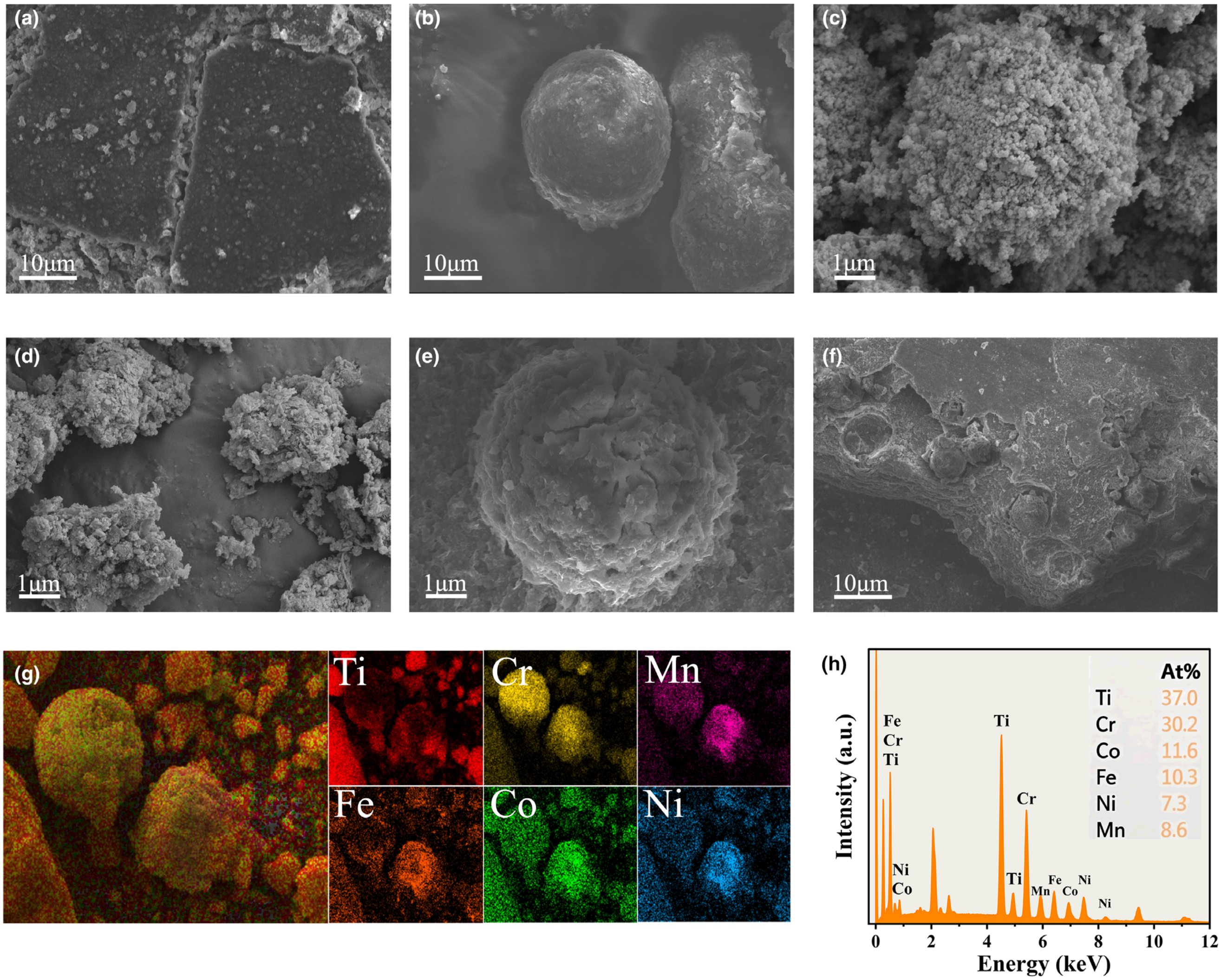

Figure 2. a) SEM images of MXene, b) HEA, c) 2-HEA@MXene, d) 8-HEA@MXene, e, f) 5-HEA@MXene; g) elemental mapping of 5-HEA@MXene for Ti, Cr, Mn, Fe, Co, and Ni, and h) EDS patterns image of 5-HEA@MXene.

distribution analysis (Figure S3, Supporting Information), the HEA@MXene composite exhibits a broad size distribution ranging from sub-micron to several hundred microns. The differential volume curve shows a sharp primary peak centered around 9.66 μm, indicating that the majority of the material consists of fine particles within an optimal range for electrode fabrication. A secondary, broader population is observed in the larger size regime. This bimodal distribution is advantageous for electrode performance, where the fine particles provide a high active surface area, and the coarser particles contribute to improved packing density and beneficial porosity in the electrode film, thereby facilitating electrolyte infiltration and ion transport.[28]

EDS was performed to investigate the elemental distribution and atomic ratios in the 5-HEA@MXene composite. As shown in Figure 2g, the elemental maps confirm the uniform distribution of Ti, Cr, Mn, Fe, Co, and Ni across the nanospheres. Further quantitative analysis (Figure 2h) reveals an atomic ratio of approximately 3:3:1:1:1:1 for these elements. This result confirmed the successful incorporation and homogeneous dispersion of the high-entropy alloy components within the composite matrix. Figure S4, Supporting Information shows a uniform distribution of Ti, C, and O on the surface while the layered MXene structure is preserved, confirming the surface generation of TiO_2 without damaging the MXene framework.

The XPS survey spectra of HEA and HEA@MXene are shown in **Figure 3a**, confirming the presence of all five HEA elements.[29] The Cr 2p spectra in Figure 3b showed peaks at 577.50 eV ($2p_{3/2}$) and 586.50 eV ($2p_{1/2}$) corresponding to Cr^{2+} species.[30] The Mn 2p spectrum was deconvoluted into contributions from Mn^{3+} and Mn^{4+} species, with the Mn 2p3/2 and Mn 2p1/2 peaks located at 642.50 eV and 654.50 eV.[31] The Fe 2p spectra in Figure 3d showed peaks at 710.25 eV and 713.03 eV representing Fe^{2+} and Fe^{3+} oxidation states, respectively, and a satellite peak was located at 717.66 eV.[32] Therefore, these samples had mixed iron valence states. The Co 2p spectra in

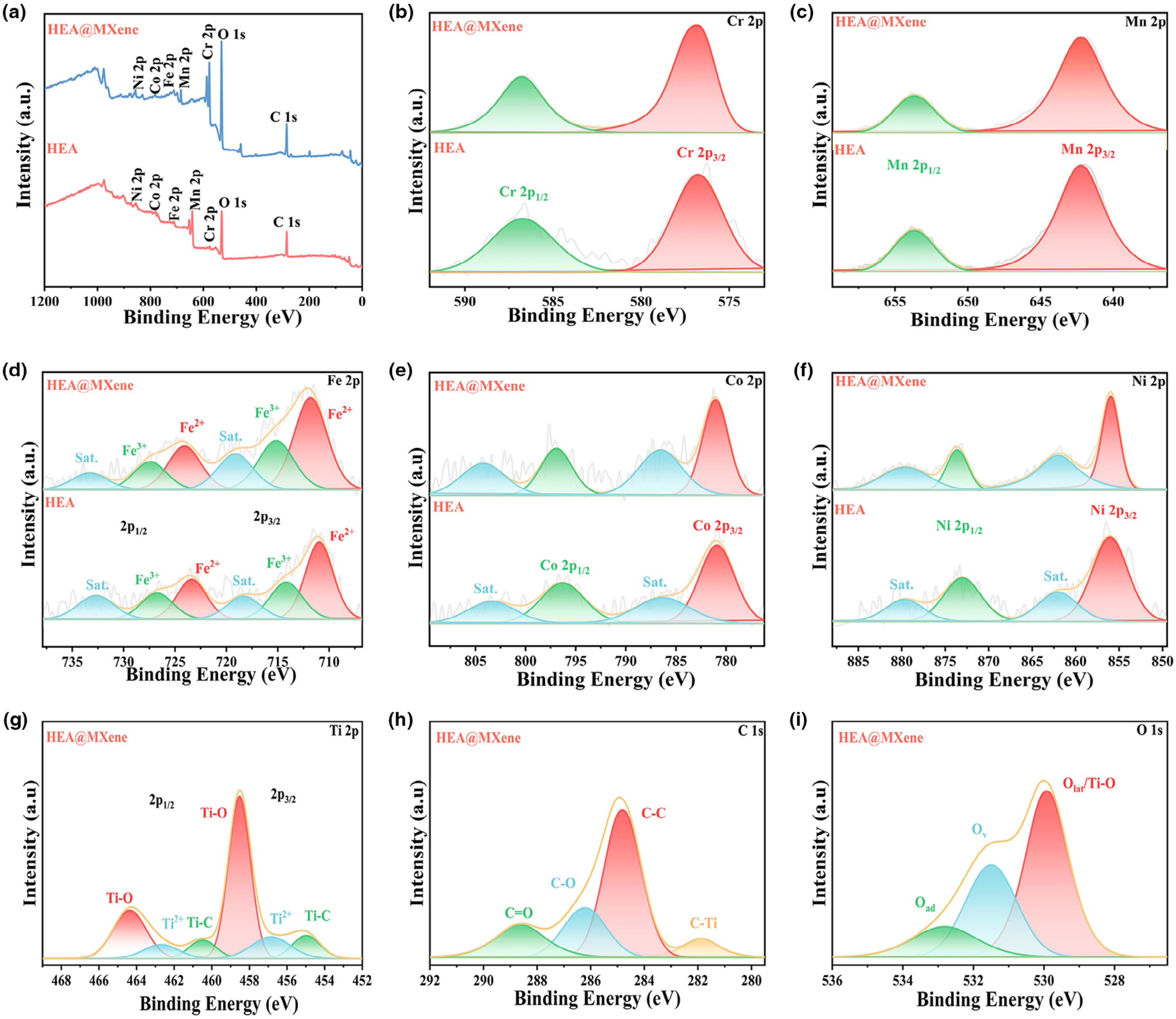

Figure 3. XPS analysis of HEA and HEA@MXene: a) survey, b) Cr 2p, c) Mn 2p, d) Fe 2p, e) Co 2p, and f) Ni 2p spectra, g) Ti 2p, h) C 1s, i) O 1s.

Figure 3e showed broad peaks at 780.79 corresponding to Co^{2+}.[33] Similarly, the Ni 2p spectra in Figure 3f showed peaks at 855.50 eV ascribed to the Ni^{3+} oxidation state.[34] Furthermore, the analysis confirmed the integrity of the MXene support. The Ti 2p spectrum (Figure 3g) showed a dominant peak at approximately 455.0 eV, attributable to the Ti-C bond, which is a definitive signature of the MXene structure.[35] The C 1s spectrum (Figure 3h) could be fitted with components including C-C (284.80 eV), C-O (286.20 eV),[36,37] and critically, C-Ti (281.90 eV), the latter further corroborating the Ti-C bonding within MXene. The O 1s spectrum (Figure 3i) displayed peaks corresponding to surface oxygen-containing functional groups such as -OH and metal-O, typical of MXene.[38] Collectively, these XPS results demonstrate the successful integration of multivalent HEA with the structurally preserved MXene support. Detailed peak-fitting parameters and quantitative atomic percentages for all detected elements (Cr, Mn, Fe, Co, Ni, Ti, C, and O) are provided in Tables S2–S9, Supporting Information.

2.2. Electrochemical Performance

The supercapacitor performance of the HEA@MXene electrode was studied in 1 M KOH solution. The CV curves of the different HEA@MXene electrodes measured at 100 mV s^{-1} are presented in **Figure 4a**. All samples exhibit quasi-rectangular shapes, characteristic of capacitive behavior. Notably, the 5-HEA@MXene electrode demonstrates the largest integrated area under the CV curve, indicating superior charge storage capacity. This enhanced performance is primarily attributed to its well-developed porous architecture, wherein the abundant micropores provide a high density of active sites for ion adsorption, thereby

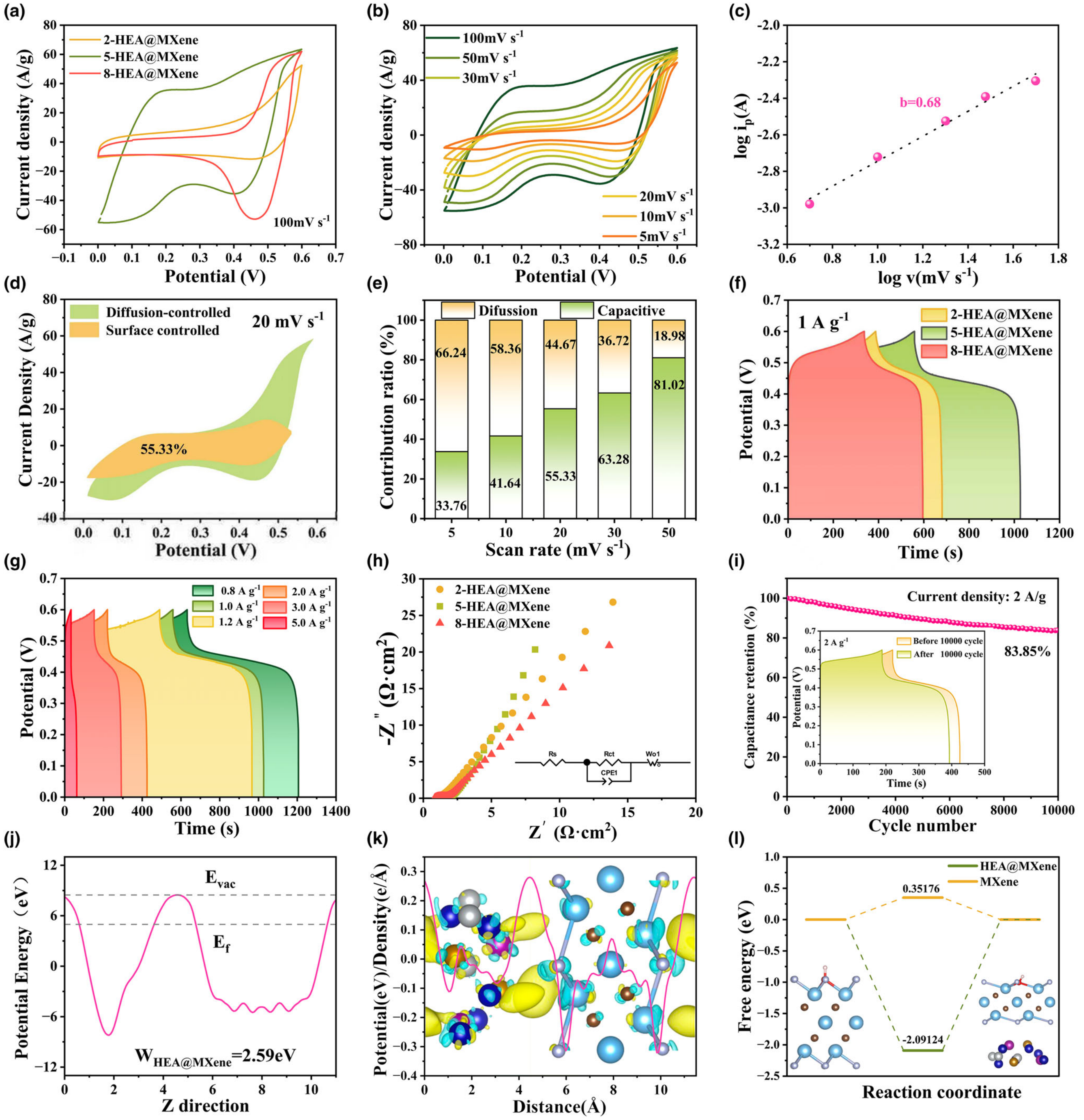

Figure 4. Electrochemical analysis of HEA@MXene electrode: a) CV curves for 2-HEA@MXene, 5-HEA@MXene, and 8-HEA@MXene; b) CV curves of 5-HEA@MXene at different sweep speeds; c) log (I) versus log(ν) plot; d) contribution of diffusion control and surface control to overall charge storage behavior at 20 mV s^{-1}; e) contribution of Q_s and Q_d at different scan rates; f) GCD curves for 2-HEA@MXene, 5-HEA@MXene, and 8-HEA@MXene; g) GCD curves of 5-HEA@MXene at different current densities; h) Nyquist plot for the three-electrode system; i) cyclic stability in three-electrode system; j) work function diagram; k) differential charge density diagram; l) comparison chart of adsorption energy changes.

contributing to its outstanding capacitive properties.[39] Figure 4b shows the CV curves of HEA@MXene from 0.0 to 0.6 V at scan rates of 5–100 mV s^{-1}. Good chemical stability was observed within this potential window (anhydrous splitting). A typical distorted rectangular shape was observed, indicating electric double-layer capacitance (EDLC) and pseudocapacitance charge-storage mechanisms. The original curve shape was maintained across all scan rates, suggesting good reversibility. Moreover, the CV curve area and current distribution increased with increasing scan rate, indicating the notable contribution of pseudocapacitance to the electrochemical charge storage properties of this electrode. The charge storage capacity of pseudocapacitive materials can be effectively characterized by a power-law relationship,[40] as shown in Equation (1):

$$I = av^{b} \tag{1}$$

The parameters a and b are adjustable constants used to characterize the charge-storage kinetics of electrode materials. This kinetic relationship can be categorized into two primary mechanisms: surface-controlled dynamics ($I \approx v$) and diffusion-controlled dynamics ($I \approx v^{-1/2}$), which collectively govern the electrochemical performance of Faraday electrodes.[41] The value of parameter "b" typically ranges from 0.5 to 1. As shown in Figure 4c, the HEA@MXene electrode had a b value of 0.68 at a potential of 0.5 V. This suggested that the mechanism for charge storage in the HEA@MXene electrode included both surface-controlled rapid Faradaic reactions and slower pseudocapacitive redox reactions driven by diffusion.[42] Specifically, the intercalation and deintercalation of K^+ ions in HEA@MXene occurred through multivalent reactive sites, which were distributed across the surface and internal regions of the electrode. This significantly enhanced its specific capacitance performance.[43]

The significant pseudocapacitive properties of HEA@MXene materials during charge storage can be ascribed to their unique mesoporous structures. In addition to shortening ion diffusion pathways, these mesoporous structures also mitigate volume expansion associated with the insertion and withdrawal of ionic species, thereby further enhancing ion transport.[44] Simultaneously, the effective contact area between the electrode and electrolyte is enhanced, further boosting charge storage efficiency. In summary, the nanostructured HEA@MXene design provided this electrode with suitable porosity, enhancing its performance. Notably, HEA@MXene showed a significantly improved specific capacitance and enhanced ion transport capacity.

At low scan rates, electrolyte ions interact extensively with electrode materials and can penetrate deeply into their internal regions, where they engage in redox reactions at polyvalent active sites. This behavior, primarily driven by intercalation/deintercalation dynamics between conductive K^+ ions and the electrode surface, results in a heightened current response dominated by diffusion-controlled mechanisms. Notably, at a scan rate of 20 mV s^{-1}, the contributions of diffusion-controlled and surface-controlled mechanisms to the charge storage behavior of HEA@MXene were 44.7% and 55.3%, respectively, as depicted in Figure 4d,e. This suggests that the electrolyte ions were engaged in slower, diffusion-controlled processes, thereby augmenting the charge storage capacity. As the scanning rate increased, the interaction time between the electrolyte ions and the electrode decreased, limiting diffusion control and favoring the surface-controlled mechanism. Overall, the delicate balance between diffusion control and surface control enabled HEA@MXene to exhibit outstanding charge storage capabilities across various scan rates.

Figure 4f displays GCD curves of HEA@MXene composites with different HEA contents. The GCD profiles reveal that the 5-HEA@MXene sample exhibits high reversibility and a notably longer discharge time, demonstrating excellent electrode conductivity. To further investigate the electrochemical performance of the 5-HEA@MXene electrode material, GCD measurements were performed within the potential window of 0–0.6 V at current densities ranging from 0.8 to 5 A g^{-1}, as shown in Figure 4g. The charge-storage properties of HEA@MXene were influenced by capacitive effects and Faraday redox reactions acting together rather than by Faraday reactions alone. At a conservative current density of 0.8 A g^{-1}, the material demonstrated an impressive specific capacitance of 893 F g^{-1}, HEA@MXene still retained 78.9% of its initial specific capacitance, confirming its good electrochemical performance.

Figure 4h compares the Nyquist plots of HEA@MXene composites with different HEA contents. The 5-HEA@MXene sample exhibits the most favorable charge transport characteristics. Equivalent circuit fitting reveals the smallest semicircle diameter in the high-frequency region, corresponding to a charge-transfer resistance (R_{ct}) of only 0.454 Ω, indicating the lowest interfacial charge-transfer resistance.[45] In comparison, the R_{ct} values for 2-HEA@MXene and 8-HEA@MXene are 0.939 Ω and 1.678 Ω, respectively. This trend clearly demonstrates the optimal synergistic effect between HEA and MXene, achieved in the 5-HEA@MXene composition.

The capacity retention of HEA@MXene was evaluated through consecutive GCD cycles at 2 A g^{-1}, as shown in Figure 4i. After 10 000 cycles, approximately 83.85% of the initial capacity was retained. To comprehensively assess the rate capability and long-term stability, further cycling tests were conducted at a higher current density of 5 A g^{-1} for 10 000 cycles (Figure S5, Supporting Information). The detailed capacitance retention percentage and Coulombic efficiency at intervals of 1000 cycles under different current densities are summarized in Table S10, Supporting Information. FESEM images of the coated electrode before and after 10 000 GCD cycles at 5 A g^{-1} are shown in Figure S6, Supporting Information. It is observed that a hydroxide layer was grown on the original morphology of HEA, while the underlying structural integrity of the particles was not significantly disrupted. This indicates remarkable morphological stability even after prolonged cycling, which is consistent with the high capacity retention. The work function is a physical quantity describing the attraction or repulsion of electrons on a material surface. As shown in Figure 4j, HEA@MXene exhibited a low work function, indicating an enhanced ability to transfer electrons from the electrode to the electrolyte.[46] This accelerated charge transfer is associated with redox reactions, leading to a pronounced boost in pseudocapacitance and overall enhanced supercapacitor performance.[47]

The differential charge density analysis in Figure 4k reveals a localized charge accumulation at the MXene-HEA interface, indicative of a specific and stable electron interaction. The presence of a charge transfer of 0.155 e$^-$ across the interface confirms a moderate yet robust bonding configuration. This optimized interfacial electronic structure contributes to the excellent mechanical and electrochemical stability of the electrode, effectively mitigating degradation during prolonged cycling and ensuring outstanding capacity retention. Moreover, adsorption is a fundamental step in electrochemical reactions, and the binding capacity between the electrode material and electrolyte ions directly governs its electrochemical performance. The adsorption energies of OH^- ions on the pristine MXene and the HEA@MXene composite were calculated to be 0.35 and −2.10 eV, respectively, as summarized in Figure 4l. The significantly more negative adsorption energy of the composite indicates a thermodynamically favorable, stronger binding interaction with OH^- ions, further demonstrating that the formation of a heterojunction enhances the electrode material's affinity toward the electrolyte.

2.3. Performance of ASC

ASC was fabricated using HEA@MXene as the cathode and activated carbon (AC) as the anode to evaluate further HEA@MXene's performance (**Figure 5**a). Figure 5b shows the CV curves of this HEA@MXene//AC device, obtained at 30 mV s^{-1} over different voltage windows, with stable operation and no discontinuities observed. Thus, the device operated up to 1.6 V. Next, CV curves were obtained over 5–100 mV s^{-1} within the stable voltage window of 0–1.6 V, as shown in Figure 5c. These CV curves maintained their near-rectangular shape with no signs of electrolyte decomposition. The unmistakable features in the CV curves indicated that the HEA material exhibited clear pseudo-capacitive behavior. GCD tests were carried out from 0.8 to 1.6 V at a rate of 2 A g^{-1}, and as depicted in Figure 5d, there were no sharp spikes or interruptions in the data. Figure 5e demonstrates that the composite delivered a specific capacitance of 204.35 F g^{-1} at 0.8 A g^{-1} and maintained 71.4% capacitance retention at 5 A g^{-1}, as measured from GCD curves over the range 0.8–5 A g^{-1}. The Nyquist plot of the ASC device is depicted in Figure 5f. The fitting results showed R_s and R_{ct} values of 3.372 $\Omega\,cm^{-2}$ and 0.807 $\Omega\,cm^{-2}$, respectively. After 10 000 cycles, the value of R_s slightly increased by 0.37 $\Omega\,cm^{-2}$, while the change in R_{ct} was negligible.

The energy and power densities of the ASC were evaluated using Equations (2) and (3), respectively.[48,49]

$$E = \frac{I\int V\mathrm{d}t}{3.6m} \tag{2}$$

$$P = \frac{E}{\Delta t} \tag{3}$$

At power densities of 0.64, 0.80, 1.20, 1.60, 2.40, and 4.00 kW kg^{-1}, the ASC had energy densities of 72.66, 65.51, 59.25, 59.16, 47.87, and 46.78 Wh kg^{-1}, respectively. Among high entropy-

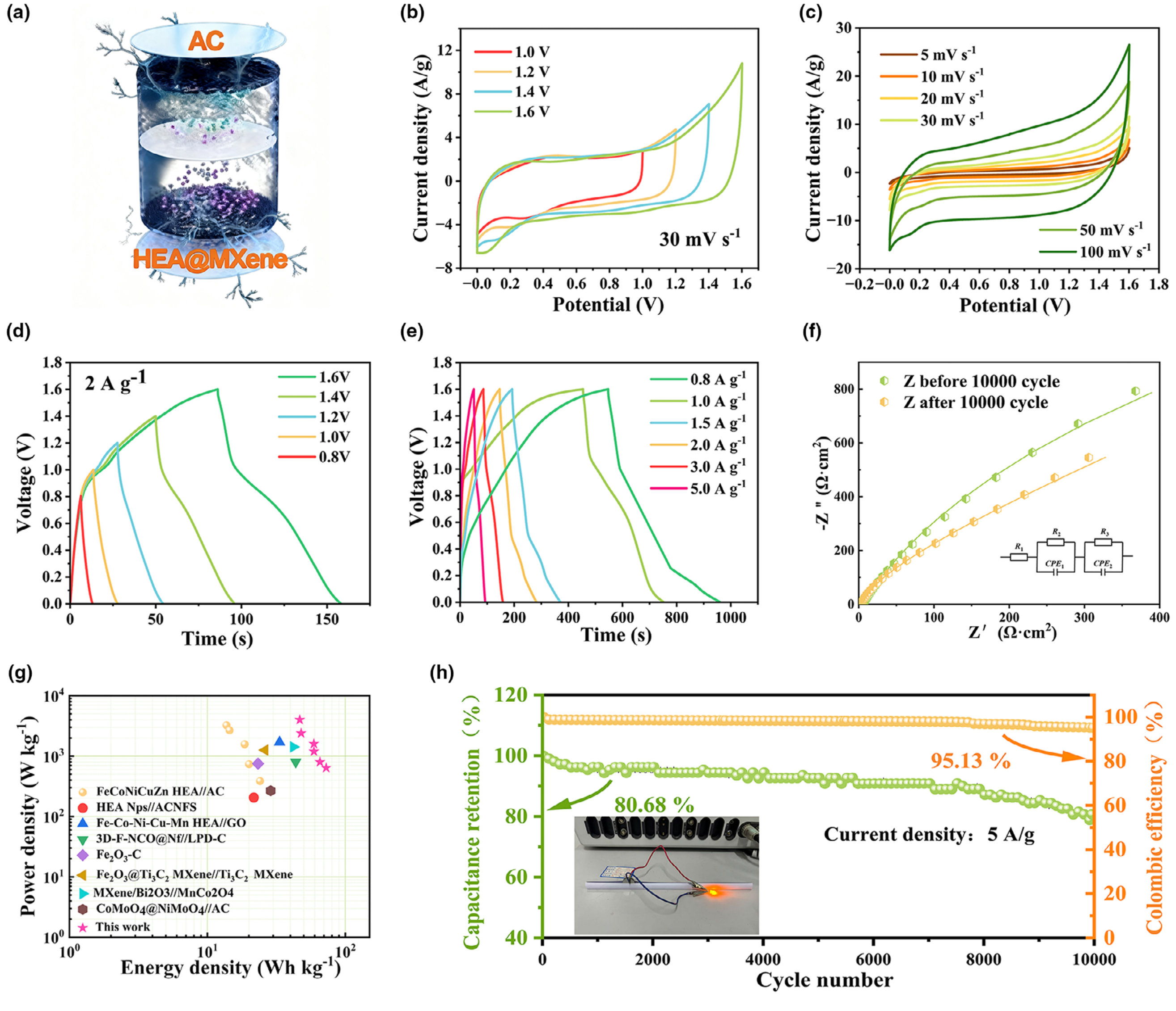

Figure 5. a) Setting diagram of HEA@MXene//AC ASC device; b) CV profiles in different potential windows; c) CV profiles at different scan rates; d) GCD profiles in different potential windows; e) GCD profiles at different current densities; f) Nyquist plot; g) Ragone plot; h) cyclic stability and capacity retention.

based supercapacitive materials, FeNiCoMnMg HEA-NPsACNFs[50] exhibit an energy density of 21.7 Wh kg^{-1}. Furthermore, when compared with various reported asymmetric supercapacitors, such as 3D-F-NCO@Nf//LPD-C (43.71 Wh kg^{-1} at 800 W kg^{-1}),[51] Fe_2O_3-C (23.30 Wh kg^{-1} at 750 W kg^{-1}),[52] the performance advantage of the HEA@MXene//AC device is evident. The Ragone diagram in Figure 5g consolidates this comparison, clearly demonstrating that this asymmetric supercapacitor outperforms both the pristine HEA material and typical metal oxide-based counterparts in terms of energy and power density. The corresponding performance comparison is summarized in Table S11, Supporting Information. This indicates that the HEA asymmetric supercapacitor has a higher energy storage capacity and a faster rate of energy release, making it potentially more suitable for high-power applications that demand long-term stability.

The cycling performance of the ASC was evaluated through consecutive GCD cycles at 5 A g^{-1}, as depicted in Figure 5h. During the first 1500 charge/discharge cycles, the capacitance retention gradually declined to 95.32%. A steady decline in capacitance was observed from 3000 to 5000 cycles, with a capacitance retention of 92.61%. Compared to typical oxide structures, the HEA@MXene electrode exhibited a higher mass loading due to its predominantly metallic matrix. After several cycles, the electrode structure degraded slightly, but stability was maintained throughout the process. After 10 000 cycles, 80.68% of the capacitance was retained.

3. Conclusions

This study reports a novel electrode material comprising HEA and MXene to enhance the energy density of supercapacitors. In a single-electrode setup with a 1 M potassium hydroxide aqueous electrolyte, HEA@MXene achieved a specific capacitance of 872 F g^{-1} at 1 A g^{-1}, indicating its exceptional performance. DFT calculations revealed that incorporating HEA significantly increased the DOS near the Fermi level, promoted interfacial charge transfer, and enhanced the adsorption energy of OH^{-} ions, thereby explaining the enhanced electrochemical performance. An asymmetric supercapacitor assembled using HEA@MXene demonstrated exceptional performance, with an energy density of 72.66 Wh kg^{-1} at a power density of 640 W kg^{-1}. This asymmetric supercapacitor also demonstrated stable cycling performance during continuous charge–discharge at 5 A g^{-1}, retaining approximately 80.68% of its capacity after 10 000 cycles. The mild synthesis conditions, tunable morphology, and enhanced regulation of electronic structure offer new insights into the design of high-performance electrode materials for next-generation supercapacitors via high-entropy alloy integration.

4. Experimental Section

Preparation of HEA@MXene: Commercially available anhydrous chromium trichloride ($CrCl_3$), anhydrous manganese chloride ($MnCl_2$), anhydrous ferric chloride ($FeCl_3$), cobalt trichloride hexahydrate ($CoCl_2{\cdot}6H_2O$), anhydrous nickel chloride ($NiCl_2$), acetylene black, lithium fluoride, hydrofluoric acid (5 wt%), and N-methyl-2-pyridone (NMP) were purchased from Shanghai Maclin Biochemical Co., Ltd. MAX powder (300 mesh) was purchased from FoShan XinXi Technology Co., Ltd. All chemicals were of analytical grade and did not require further processing.

Synthesis of HEA: Cr-Mn-Fe-Co-Ni HEA was prepared by sealed induction melting using $CrCl_3$, $MnCl_2$, $FeCl_3$, $CoCl_2{\cdot}6H_2O$, and $NiCl_2$ as raw materials.[53] A 0.2 mmol equimolar mixture of chromium, manganese, iron, cobalt, and nickel was sealed under argon and induction melted at 1350 °C. The resulting ingot was melted and solidified several times to achieve uniformity. To achieve further homogenization, the product was calcined at 800 °C for 3 hours in a tube furnace, with a heating rate of 5 °C min^{-1} under a continuous N_2 flow.

Preparation of HEA@MXene: Ten milliliters of MXene (~5 mg mL^{-1}) was centrifuged at 6000 rpm for 10 min to collect the precipitate. The MXene precipitate was then added to 20 mL of deionized water and magnetically stirred for 10 min. Next, 0.75 mL of a 1 M HCl solution was added, and stirring was continued for an additional 30 min until the mixture turned into a clear, transparent, light-yellow solution (with a pH of approximately 2). Aliquots of the resulting solution were transferred to 100 mL Teflon-lined autoclaves, followed by the addition of 0.02, 0.05, and 0.08 g of HEA powder (corresponding to HEA-to-MXene mass ratios of approximately 0.4:1, 1:1, and 1.6:1, respectively, based on 0.05 g of MXene). The suspensions were then sonicated for 30 min, and the hydrothermal reaction was performed at 180 °C for 24 h.

After naturally cooling to room temperature, the black products were collected by centrifugation at 8000 rpm for 10 min. The collected precipitates were sequentially washed three times with 0.1 M HCl solution (20 mL each), deionized water (20 mL each, until the supernatant reached pH ~ 6), and anhydrous ethanol (20 mL each) to remove residual ions and by-products. Finally, the purified solids were transferred to a vacuum drying oven and dried at 60 °C for 12 hours, yielding the final products denoted as 2-HEA@MXene, 5-HEA@MXene, and 8-HEA@MXene, corresponding to the initial HEA mass added.

Material characterization: Crystal structures were analyzed via X-ray diffraction (XRD) using a Panalytical Empyrean diffractometer with Cu Kα radiation within the 2θ range of 5° to 80°. The morphologies and elemental distributions of the samples were evaluated using scanning electron microscopy (SEM) on an Apreo 2C. Elemental composition and valence states were studied using X-ray photoelectron spectroscopy (XPS) with a Thermo ESCALAB 250Xi. Nitrogen adsorption–desorption analysis was used to obtain the Brunauer–Emmett–Teller (BET) specific surface area and pore structure of the materials. Fourier transform infrared spectroscopy (FTIR) was utilized to study surface functional groups.

Electrochemical measurements: The electrochemical evaluation of the supercapacitor materials was performed on a Metrohm instrument. Each electrode was prepared with 80% active material (HEA@MXene powder), 10% carbon black as the conductive agent, and 10% PVDF as the binder. These components were combined into a slurry using *N*-methyl-2-pyrrolidone (NMP) as a solvent. The slurry was ground with a mortar and then sonicated for 30 min to achieve uniformity. Next, the slurry was coated onto pre-cleaned (acetone-washed) nickel foam sheets (1×2 cm^2 area, 0.2 mm thickness), and the sheets were dried overnight at 60 °C under vacuum. A three-electrode system was utilized for the electrochemical tests. The coated nickel foam was used as the working electrode, an Ag/AgCl electrode served as the reference, and a platinum wire functioned as the counter electrode. The mass of active material (HEA@MXene) coated on each nickel foam electrode was approximately 2.0 mg. All specific capacitance, energy density, and power density values reported are calculated based on the mass of the active material.

Computational methodology: DFT calculations were performed using the Vienna Ab initio Simulation Package (VASP).[54] The electron projection augmented wave (PAW) pseudopotential was used to describe electron-ion interactions. The Perdew–Burke–Ernzerhof (PBE) generalized gradient approximation (GGA) was adopted to describe electron exchange and correlation effects.[55] A Monte Carlo special quasirandom structure (MCSQS) was used to avoid extreme asymmetry or highly repetitive structures by randomly assigning different elements to different lattice positions, while ensuring that the local structure of the system changed regularly.[56] The Monte Carlo method was used to optimize the structure, ensuring that the atomic arrangement reached thermodynamic equilibrium. With this method, various configurations were effectively simulated, yielding stable, low-energy structures. In simulations examining hydroxyl adsorption, a 15 Å vacuum layer was introduced along the c-axis to avoid interactions between adjacent layers. The Brillouin zone at the R point was utilized to monitor nanocluster relaxation. For DOS calculations, a $6 \times 6 \times 1$ Monkhorst-Pack grid was used. An energy cutoff of 500 eV was used for plane-wave selection. The conjugate gradient method was iterated until convergence, with the energy and force criteria reaching 10^{-5} eV and 0.01 eV $Å^{-1}$, respectively.

Acknowledgements

The authors acknowledge the financial support provided by the National Natural Science Foundation of China (Grant No. 52206220), the Key Technology Research and Development Plan of Jilin Province (Grant No. 20240304098SF), and Science and Technology Project of China Huaneng Group (Grant No. HNKJ25-H89). We would like to thank MogoEdit (https://www.mogoedit.com) for its English editing during the preparation of this manuscript.

Conflict of Interest

The authors declare no conflict of interest.

Supporting Information

Supporting Information is available from the Wiley Online Library or from the author.

Keywords

DFT, electrode materials, high-entropy alloy (HEA), MXene, supercapacitor

Received: February 15, 2026
Revised: April 9, 2026
Published online: April 14, 2026

---

[1] W. Li, Z. Wang, Y. Zhu, Y. Zhao, K. Zhang, A. Qin, S. Chen, *Chem. Eng. J.* **2025**, *527*, 171594.
[2] N. Choudhary, C. Li, J. Moore, N. Nagaiah, L. Zhai, Y. Jung, J. Thomas, *Adv. Mater.* **2017**, *29*, 1605336.
[3] J. Sun, C. Wu, X. Sun, H. Hu, C. Zhi, L. Hou, C. Yuan, *J. Mater. Chem. A* **2017**, *5*, 9443.
[4] X. Yao, Z. Zhang, W. Deng, C. Feng, Q. Xu, X. Lin, Z. Peng, Y. Cao, W. Guo, B. L. Khoo, S. Wang, *Adv. Sci.* **2025**, *12*, e08650.
[5] S. M. Z. Mehdi, H. G. Abbas, M. Ali, S. B. H. Rizvi, S. R. Choi, J. C. Goak, Y. Seo, S. Kumar, N. Lee, *Energy Environ. Mater.* **2025**, *8*, e12876.
[6] J. Dong, Z. Lu, L. Hua, Z. Guo, X. Xu, J. Wu, F. Jia, Y. Wang, *Nano-Micro Lett.* **2026**, *18*, 158.
[7] Y. Y. Chen, T. Duval, U. D. Hung, J. W. Yeh, H. C. Shih, *Corros. Sci.* **2005**, *47*, 2257.
[8] X. Wang, W. Guo, Y. Fu, *J. Mater. Chem. A* **2021**, *9*, 663.
[9] B. X. Cao, C. Wang, T. Yang, C. T. Liu, *Scr. Mater.* **2020**, *187*, 250.
[10] M. S. Lal, R. Sundara, *ACS Appl. Mater. Interfaces* **2019**, *11*, 30846.
[11] S. Zhang, J. Huang, J. Tang, Z. Liu, X. Deng, *Appl. Surf. Sci.* **2024**, *667*, 160417.
[12] G. C. Mohanty, C. Chowde Gowda, P. Gakhad, A. Verma, S. Das, S. Chowdhary, J. Bhattacharya, A. K. Singh, K. Biswas, C. S. Tiwary, *Energy Storage.* **2024**, *6*, e668.
[13] G. Laplanche, A. Kostka, C. Reinhart, J. Hunfeld, G. Eggeler, E. P. George, *Acta Mater.* **2017**, *128*, 292.
[14] S. K. Nemani, B. Zhang, B. C. Wyatt, Z. D. Hood, S. Manna, R. Khaledialidusti, W. Hong, M. G. Sternberg, S. K. R. S. Sankaranarayanan, B. Anasori, *ACS Nano* **2021**, *15*, 12815.
[15] H. T. A. Awan, A. A. Aboalhassan, M. A. A. M. Abdah, M. N. Mustafa, N. M. Saidi, R. Walvekar, M. Khalid, *Batter. Energy* **2026**, *5*, e70086.
[16] Y. Xin, M. Zhu, H. Zhang, X. Wang, *Nano-Micro Lett.* **2026**, *18*(1), 1.
[17] A. S. Etman, J. Zhou, J. Rosen, *Electrochem. Commun.* **2022**, *137*, 107264.
[18] W. Ma, Z. Qiu, M. Wang, C. Tan, L. Hu, X. Lv, Q. Li, J. Li, J. Dang, *Scr. Mater.* **2023**, *235*, 115596.
[19] K. Manoharan, M. Pumera, *NPJ Flexible Electron.* **2025**, *9*, 120.
[20] N. M. Shinde, M. Pumera, *Energy Fuel* **2025**, *39*, 21583.
[21] S. Mathew, K. R. P. Sunajadevi, D. Pinheiro, *Mater. Adv.* **2025**, *6*, 7207.
[22] X. Jin, X. Gu, F. Quan, X. Ran, K. Zhang, A. Mao, *Mater. wiss. Werkst. tech.* **2019**, *50*, 837.
[23] S. Xu, C. Zhao, G. Li, Z. Shi, B. Liu, *RSC Adv.* **2023**, *13*, 15843.
[24] M. A. K. Purbayanto, M. Chandel, D. Bury, A. Wójcik, D. Moszczyńska, A. Tabassum, V. N. Mochalin, M. Naguib, A. M. Jastrzębska, *Langmuir* **2024**, *40*, 21547.
[25] C. E. Park, R. A. Senthil, G. H. Jeong, M. Y. Choi, *Small* **2023**, *19*, 2207820.
[26] D. Gandla, Q. Li, Y. Zhou, Y. Yan, Z. Liu, J. Chen, D. Q. Tan, *Small* **2024**, *20*, 2404880.
[27] M. Z. Ansari, S. A. Ansari, N. Parveen, M. W. Alam, S. H. Kim, *J. Energy Storage* **2025**, *131*, 117535.
[28] W. Chung, H. Lee, J. H. Shim, J. H. Bang, *J. Electrochem. Sci. Technol.* **2025**, *16*, 512.
[29] E. Shen, X. Song, Q. Chen, M. Zheng, J. Bian, H. Liu, *ChemElectroChem* **2021**, *8*, 260.
[30] B. Talluri, M. L. Aparna, N. Sreenivasulu, S. S. Bhattacharya, T. Thomas, *J. Energy Storage* **2021**, *42*, 103004.
[31] S. A. Ansari, *J. Power Sources* **2025**, *646*, 237185.
[32] M. Nawwar, R. Poon, R. Chen, R. P. Sahu, I. K. Puri, I. Zhitomirsky, *Carbon Energy* **2019**, *1*, 124.
[33] S. G. Çolak, A. Güngör, M. Ö. A. Çolak, U. B. Şimşek, R. G. Altürk, E. Erdem, *J. Colloid Interface Sci.* **2025**, *701*, 138672.
[34] A. H. Phakatkar, M. T. Saray, M. G. Rasul, L. V. Sorokina, T. G. Ritter, T. Shokuhfar, R. Shahbazian-Yassar, *Langmuir* **2021**, *37*, 9059.
[35] M. C. Biesinger, L. W. Lau, A. R. Gerson, R. S. C. Smart, *Appl. Surf. Sci.* **2010**, *257*, 887.
[36] N. Parveen, S. A. Ansari, K. M. Alnahdi, H. H. Hammud, W. A. Aljamhi, M. W. Alam, S. F. Adil, W. A. Zoubi, *J. Photochem. Photobiol. A Chem.* **2025**, *459*, 116096.
[37] J. Halim, K. M. Cook, M. Naguib, P. Eklund, Y. Gogotsi, J. Rosen, M. W. Barsoum, *Appl. Surf. Sci.* **2016**, *362*, 406.
[38] J. Halim, S. Kota, M. R. Lukatskaya, M. Naguib, M.-Q. Zhao, E. J. Moon, J. Pitock, J. Nanda, S. J. May, Y. Gogotsi, M. W. Barsoum, *Adv. Funct. Mater.* **2016**, *26*, 3118.
[39] S. A. Ansari, N. Parveen, M. Z. Ansari, G. M. Alsulaim, M. W. Alam, M. Y. Khan, A. Umar, I. Hussain, K. Zhang, *Prog. Mater. Sci.* **2025**, *154*, 101493.
[40] C. Ni, X. Wang, X. Cai, Q. Wu, Y. Shen, C. Hao, *J. Mater. Sci. Technol.* **2025**, *210*, 233.
[41] M. Saraf, C. E. Shuck, N. Norouzi, K. Matthews, A. Inman, T. Zhang, E. Pomerantseva, Y. Gogotsi, *Energy Environ. Mater.* **2023**, *6*, e12516.
[42] E. Noormohammadi, L. Naji, *Chem. Eng. J.* **2025**, *526*, 171371.
[43] S. Xu, Y. Li, T. Mo, G. Wei, Y. Yang, *Energy Storage Mater.* **2024**, *69*, 103379.
[44] X. Yan, Y. Zhou, S. Wang, *Adv. Funct. Mater.* **2025**, *35*, 2413115.
[45] S. A. Ansari, M. W. Alam, A. BaQais, M. A. Yewale, *J. Ind. Eng. Chem.* **2025**, *155*, 788.
[46] S. Ningshen, U. K. Mudali, B. Raj, *Corros. Rev.* **2009**, *27*, 493.
[47] J. Li, Z. Li, X. Liu, C. Li, Y. Zheng, K. W. K. Yeung, Z. Cui, Y. Liang, S. Zhu, W. Hu, Y. Qi, T. Zhang, X. Wang, S. Wu, *Nat. Commun.* **2021**, *12*, 1224.
[48] B. T. Al-Abawi, N. Parveen, S. A. Ansari, H. A. Al-Dosari, H. K. Alshaikh, A. Umar, A. A. Ibrahim, S. Akbar, *Int. J. Energy Res.* **2025**, *2025*, 5331742.
[49] E. Baasanjav, K. A. S. Raj, H. Hakkeem, C. S. Rout, S. M. Jeong, *J. Mater. Sci. Technol.* **2025**, *228*, 42.
[50] X. Xu, Y. Du, C. Wang, Y. Guo, J. Zou, K. Zhou, Z. Zeng, Y. Liu, L. Li, *J. Alloys Compd.* **2020**, *822*, 153642.
[51] N. Parveen, *J. Ind. Eng. Chem.* **2025**, *150*, 824.
[52] N. Parveen, E. Da'na, A. Taha, *Nanotechnology* **2025**, *36*, 115704.

[53] S. Das, M. Sanjay, A. R. S. Gautam, R. Behera, C. S. Tiwary, S. Chowdhury, *J. Environ. Manag.* **2023**, *342*, 118081.

[54] G. Kresse, J. Hafner, *Phys. Rev. B* **1993**, *47*, 558.

[55] G. Kresse, D. Joubert, *Phys. Rev. B* **1999**, *59*, 1758.

[56] A. H. Larsen, J. J. Mortensen, J. Blomqvist, I. E. Castelli, R. Christensen, M. Dulak, J. Friis, M. N. Groves, B. Hammer, C. Hargus, E. D. Hermes, P. C. Jennings, P. B. Jensen, J. Kermode, J. R. Kitchin, E. L. Kolsbjerg, J. Kubal, K. Kaasbjerg, S. Lysgaard, J. B. Maronsson, T. Maxson, T. Olsen, L. Pastewka, A. Peterson, C. Rostgaard, J. Schiøtz, O. Schütt, M. Strange, K. S. Thygesen, T. Vegge, L. Vilhelmsen, M. Walter, Z. Zeng, K. W. Jacobsen, *J. Phys. Condens. Matter* **2017**, 29, 273002.